# Perturbation Observer-Based Nonlinear Control of VSC-MTDC Systems

Weiyu Wang, Xin Yin, Lin Jiang, Yijia Cao, and Yong Li

***Abstract*—The voltage source converter based multi-terminal direct-current (VSC-MTDC) system is a promising technique to integrate multiple large offshore wind farms (OWF) and to share the power between multiple ac grids. The operation and control of VSC-MTDC systems could be affected by multiple uncertainties, e.g., the stochastic power generation of OWFs, nonlinearities of VSC-MTDC systems and unknown dynamics triggered by grid faults, which may result in poor dynamic performance and stability issues. In this paper, a perturbation observer-based nonlinear control (PONC) is proposed to improve the robustness of VSC-MTDC systems with OWFs. The perturbation observer is designed to estimate the lumped perturbation terms, which include all the system uncertainties, unknown dynamics and the external disturbances together with the state estimates. Based on the estimated perturbation and states, the output feedback linearization controllers are designed to compensate the impact of the lumped perturbation and to achieve robust tracking performance, without requiring the accurate system model. The effectiveness of PONC is verified by a 5-terminal VSC-MTDC system.**

***Index Terms*—VSC-MTDC, offshore wind farms, feedback linearization control, robustness, fault ride-through, high gain observer, output feedback control.**

## NOMENCLATURE

| | |
|---|---|
| $C_{eq}, C_{mmc}$ | equivalent dc-link capacitor, capacitance of one submodule of VSC-stations |
| $V_{dc}, V_{eq}$ | dc voltage of the $C_{eq}$ and VSC-stations |
| $R_{dc}, L_{dc}$ | aggregated resistance and inductance of converters |
| $R_{arm}, L_{arm}$ | equivalent resistance and inductance of one arm |
| $V_t, V_o, V_g$ | ac voltage of converter, filter capacitor, and the ac grid |
| $I_t, I_o$ | ac current output of converter, filter |
| $R_f, L_f$ | aggregated impedance of transformer and filter |
| $R_g, L_g$ | lumped resistance and inductance of the transmission lines |
| $\omega$ | angular frequency of ac grids |
| $P_m$ | pulse-width modulator signal |
| $P_o, Q_o$ | active and reactive power output through the filter |
| $\mathbf{f}, \mathbf{k}, \mathbf{g}, \mathbf{h}$ | nonlinear function vectors |
| $\mathbf{x}, \mathbf{u}, \mathbf{y}, \mathbf{D}$ | state vector, input vector, output vector, measured disturbance vector |
| $\mathbf{L}$ | Lie derivative |
| $\alpha, \beta$ | Lie derivatives vector |
| $v$ | auxiliary control input signal |
| $\mathbf{z}$ | state vector of the equivalent linear model |
| $\hat{\mathbf{z}}$ | estimated value of $\mathbf{z}$ |
| $\tilde{\mathbf{z}}$ | estimation error of $\mathbf{z}$ |
| $\eta$ | scaled estimation error of $\mathbf{z}$ |
| $\mathbf{A}, \mathbf{B}$ | state matrix and input matrix of the equivalent linear model |
| $k$ | feedback control gain |
| $p$ | lumped perturbation |
| $\mathbf{p}$ | perturbation matrix |
| $P_{oref}, Q_{oref}$ | reference of active and reactive power |
| $K_v$ | $P-V$ droop coefficient |
| $\varepsilon$ | small constant of observer |
| $h$ | observer gain |

**Subscripts**

| | |
|---|---|
| $a, b, c$ | three-phase components |
| $d, q$ | $d$- and $q$-axis components |
| $wf, gs$ | variables related to WFVSC and GSVSC |
| 0 | initial value |
| $ref$ | reference value |

**Abbreviation**

| | |
|---|---|
| VSC | votlage source converter |
| MTDC | multi-terminal direct current |
| WFVSC | wind farm-side VSC-station |
| GSVSC | grid-side VSC-station |
| OWF | offshore wind farm |

W. Wang and Y. Cao are with the School of Electrical and Information Engineering, Changsha University of Science & Technology, Changsha, 410000, China, (e-mail: WYWang@csust.edu.cn, yjcaohnu@163.cn).

L. Jiang and X. Yin are with the Department of Electrical Engineering and Electronics, University of Liverpool, Liverpool L69 3GJ, U.K. (e-mail: ljiang@liv.ac.uk, xin.yin@liverpool.ac.uk).

Y. Li is with the College of Electrical and Information Engineering, Hunan University, Changsha, 410114, China, (email: yongli@hnu.edu.cn).

## I. INTRODUCTION

OFFSHORE wind farms (OWFs) have drawn much attention in recent years due to the small footprint, high wind speed and high annual utilization hours [1]. Owing to the technical and economical feasibility, the voltage source converter-based multi-terminal direct current (VSC-MTDC) system is preferred to integrate with multiple large scale OWFs and for the interconnection of multiple onshore ac grids [2].

Although the large scale OWFs can provide considerable power generation to the on shore ac grids, the stochastic and fluctuation of wind energy and the complex system dynamics pose several challenges on the control and operation of VSC-MTDC systems:

1) The intermittent power generation of wind generators could results in the ac voltage fluctuation of OWFs, which can reduce the efficiency and stability of OWFs [3].

2) The accurate model of VSC-MTDC systems is hard to be obtained, especially the modular multilevel converter (MMC) based MTDC systems. The unknown dynamics, parameter uncertainties and time-varying operation points could result in tracking error [4].
3) The ac-side short-circuit faults have significant impact on the stability and security of VSC-MTDC systems.

To counter these challenges, the controllers of VSC-MTDC systems are required to have superior dynamic performance against the stochastic operating conditions, system uncertainties and external disturbances.

A VSC-MTDC system used for the integration of OWFs generally have two groups of VSC-stations: wind farm-side VSC-stations (WFVSC) and grid-side VSC-stations (GSVSC). WFVSCs absorb all the power generation of OWFs and secure the voltage stability of OWFs [5]. GSVSCs aim at power-sharing between several onshore ac grids and securing the stability of dc-link voltage, which is essential to the stable operation of VSC-MTDC systems. The power output of GSVSCs have to change with the power generation of OWFs timely to secure the power balance in dc grids. Otherwise, the power imbalance in dc grid will cause the severe dc voltage deviation, which can damage the power electronics and even lead to instability [6].

There has been considerable interests in designing the control strategies of VSC-MTDC systems based on the vector control technique, such as the master-slave control, dc voltage droop control [7]–[9]. The proportional–integral (PI) regulator and the feed-forward compensator are broadly chosen as the fundamental components to construct the vector controllers, which can decouple the control of active and reactive power [10]. Based on the vector controller, the secondary control layer can be further designed to achieve ancillary services, such as frequency support [11]–[13], oscillation damping [14], [15], and fault-ride through (FRT) capability [16], [17].

However, the aforementioned references did not consider the impact of system time-varying operation points. The controller parameters tuned at a specific system operating equilibrium cannot always achieve the satisfactory performance at other operating points, especially in the stochastic operating conditions. To tackle this problem, nonlinear control approaches, such as Lyapunov function-based control, feedback linearization control, sliding-mode control, nonlinear model predictive control, are employed to improve the dynamic performance of VSC-MTDC systems [18]–[28]. In [18]–[21], Lyapunov function-based control strategies is proposed to secure the transient stability of hybrid ac/dc power systems by regulating the power output of VSC-MTDC systems. These control strategies are centralized and require the global measurements, which could introduce the communication latency and deteriorate the control performance. In [22], [23], sliding-mode control are used to compensate the nonlinearties of converters and improve the robustness against external disturbances. However, the switching actions of sliding-mode control could lead to high-frequency vibrations, which may increase the switching losses of power electronics. In [24]–[27], model predict control is used to improve the ac/dc voltage regulation and power regulation ability of VSC-HVDC/MTDC systems. However, the control performance of model predict control is highly dependent on the accuracy of the system model, which could be degraded by modeling uncertainties. In [28], the feedback linearization and zero dynamics techniques are employed to regulate the dc voltage and power output of converters. Nevertheless, the controllers proposed in [18]–[28] have not addressed the impact of multiple disturbances on the dynamics of VSC-MTDC systems.

In recent decades, there has been considerable interest in designing observer-based nonlinear controllers which can estimate and compensate the system uncertainties and external perturbations. These controllers, including the passive control, perturbation observer-based control, and adaptive control, can significantly improve the dynamic performance of renewable energies [29]–[33] and VSC-HVDC/MTDC systems [34]–[38]. Yang et al. [34]–[36] designed the passive controller and perturbation observer-based sliding-mode control for VSC-MTDC and VSC-HVDC systems. In [34], the sliding mode and perturbation observer are combined to estimate the comprehensive effect of multiple perturbations of VSC-HVDC systems. The inherent feature of perturbation rejection ensures a better robustness and tracking accuracy than that of the nonlinear adaptive control [39]. In [35], [36], a passive control strategy is designed to enhance the transient dynamics of VSC-MTDC systems. The storage function is derived and reshaped to enhance the damping of converters. The aforementioned control strategies provide superior improvement of the dynamics of VSC-HVDC/MTDC systems. However, converters could be damaged by large current under severe faults if the current control loop is eliminated. Moreover, only one GSVSC is considered to regulate the dc voltage and the coordination between multiple GSVSCs are not discussed. In [37], a current sensor-less controller, which replace the conventional current controller, is proposed for VSC-MTDC systems to improve its robustness. However, converters could be damaged by large current under severe faults if the current control loop is eliminated. A nonlinear generalized predictive control and disturbance observer has been designed for improving the stability of hybrid power systems with series and parallel compensators [38]. However, the references mentioned above have not considered the specific control targets of WFVSCs. Hence the voltage stability of the wind farms and the coordination between multiple GSVSCs are not discussed.

This paper proposes a perturbation observer-based nonlinear control (PONC) of VSC-MTDC systems. The PONC consists of the high gain observer (HGOB) and the output feedback linearization controllers (FLC). The HGOBs are designed for WFVSCs and GSVSCs to estimate the effects of the lumped perturbation, which includes the model and parameter uncertainties, converter nonlinearities, cross-coupling between of $d$- and $q$-axis subsystems and the external disturbances. Based on the perturbation estimation, the FLCs are designed to compensate the lumped perturbation and to achieve robust reference tracking. According to the proposed PONC, both the $d$- and $q$-axis voltages of WFVSCs and currents of GSVSCs are well decoupled, respectively. The voltage stability of OWFs is significantly improved and the robustness of the inner current control of GSVSCs against the lumped

perturbations are enhanced. The performance of the proposed controller is verified in a 5-terminal VSC-MTDC system in DIgSILENT/PowerFactory.

The rest of this paper is organized as follows. The nonlinear model of VSC-stations are introduced in Section II. The proposed PONC is elaborated in Section III. In Section IV, the performance of the proposed controller is verified by simulations. Section V concludes the findings of this paper.

## II. System Modeling and Conventional Vector Controller

The general configuration of a VSC-MTDC system connecting with multiple ac grids and OWFs is shown in Fig. 1. WFVSCs operate in rectifier mode and absorb all the wind power from OWFs. GSVSCs operate in inverter mode and distribute the power to ac grids. WFVSCs and GSVSCs have the same converter model, while the control targets and the controllers are different. In this section, the model of VSC-stations and the conventional vector controller (VC) will be introduced.

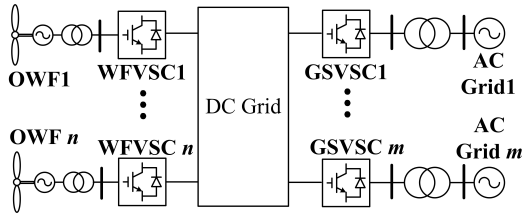


Fig. 1: General configuration of VSC-MTDC systems.

### A. Averaged-Value Model of VSC-stations

The nonlinear model of VSC-stations is formulated in $dq$ reference frame. The equivalent averaged-value model (AVM) is widely used in modeling of MMCs due to the high accuracy and the less computational burden [40]–[42]. A VSC-station can be represented by a controlled current source in the dc-side and by a controlled voltage source with an LCL-filter in the ac-side, as shown in Fig. 2.

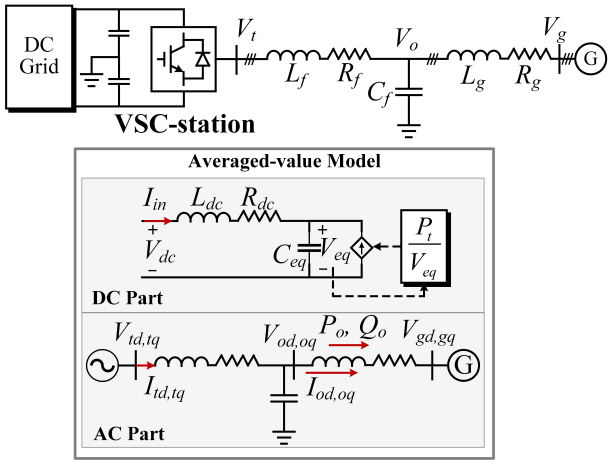


Fig. 2: The equivalent averaged-value model of VSC-stations.

The dc-side dynamics of VSC-stations can be represented by the following equations: [41]

$$\begin{cases} \dot{V}_{eq} = \dfrac{1}{C_{eq}}(I_{in} - \dfrac{P_t}{V_{eq}}) \\ \dot{I}_{in} = \dfrac{1}{L_{dc}}(V_{dc} - V_{eq} - R_{dc}I_{in}) \\ P_t = V_{td}I_{td} + V_{tq}I_{tq} \end{cases} \tag{1}$$

where $C_{eq}$ denotes the equivalent dc-link capacitor of VSC-stations, $C_{eq}$ =6$C_{mmc}/N$, where $C_{mmc}$ is the capacitance of one submodule, and $N$ is number of submodules in each arm; $V_{eq}$ is the dc voltage of the $C_{eq}$; $V_{dc}$ is the dc voltage of VSC-stations; $R_{dc}$ and $L_{dc}$ represent the aggregated resistance and inductance of the converter, which is given by $R_{dc} = (2/3)R_{arm}$ and $L_{dc} = (2/3)L_{arm}$, where $R_{arm}$ and $L_{arm}$ are the equivalent resistance and inductance of one arm; $P_t$ is the active power output of the converter; $V_{td}$, $I_{td}$, $V_{tq}$, and $I_{tq}$ are the $d$- and $q$-axis components of the voltage and current at the ac-terminal of converters.

The ac-side dynamics of VSC-stations expressed in $dq$ reference frame can be derived as [41], [42]

$$\begin{cases} \dot{I}_{td} = -\dfrac{R_f}{L_f}I_{td} + \omega I_{tq} + \dfrac{1}{L_f}(V_{td} - V_{od}) \\ \dot{I}_{tq} = -\dfrac{R_f}{L_f}I_{tq} - \omega I_{td} + \dfrac{1}{L_f}(V_{tq} - V_{oq}) \\ \dot{V}_{od} = \omega V_{oq} + \dfrac{1}{C_f}I_{td} - \dfrac{1}{C_f}I_{od} \\ \dot{V}_{oq} = -\omega V_{od} + \dfrac{1}{C_f}I_{tq} - \dfrac{1}{C_f}I_{oq} \\ \dot{I}_{od} = -\dfrac{R_g}{L_g}I_{od} + \omega I_{oq} + \dfrac{1}{L_g}(V_{od} - V_{gd}) \\ \dot{I}_{oq} = -\dfrac{R_g}{L_g}I_{oq} - \omega I_{od} + \dfrac{1}{L_g}(V_{oq} - V_{gq}) \\ V_{td} = P_{md}V_{eq} \\ V_{tq} = P_{mq}V_{eq} \end{cases} \tag{2}$$

where $R_f$ and $L_f$ represent the impedance of transformer and filter; $\omega$ is the angular frequency of the adjacent ac grid; $V_{od}$, $I_{od}$, $V_{oq}$, and $I_{oq}$ are the $d$- and $q$-axis components of the voltage and current at the point of common coupling (PCC); $R_g$ and $L_g$ represent the lumped resistance and inductance of the transmission lines; $V_{gd}$ and $V_{gq}$ are the $d$ and $q$-axis components of the grid voltage; $\omega$ is the angular frequency of the adjacent ac grid; $P_{md}$ and $P_{mq}$ are the $d$- and $q$-axis components of the pulse-width modulator (PWM) signal.

The active and reactive power output passed through the LCL-filter can be calculated by

$$\begin{cases} P_o = V_{od}I_{od} + V_{oq}I_{oq} \\ Q_o = -V_{od}I_{oq} + V_{oq}I_{od} \end{cases} \tag{3}$$

### B. Conventional Vector Controller of VSC-MTDC Systems

The conventional vector controller of WFVSCs and GSVSCs are shown in Figs. 3 and 4. WFVSCs aims at regulating the ac voltage of wind farms and GSVSCs either regulate the dc voltage of or the power output. However, both

the VCs of WFVSCs and GSVSCs rely on the proportional-integral compensator. More details about the VC can refer to [5], [7].

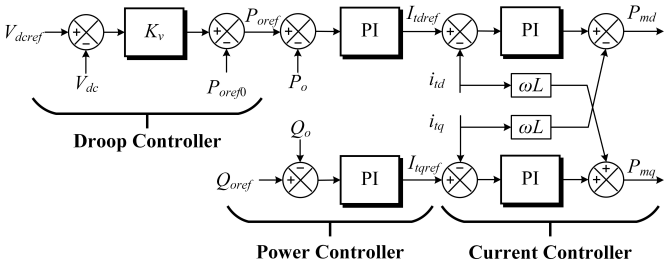


Fig. 3: Vector controller of GSVSCs.

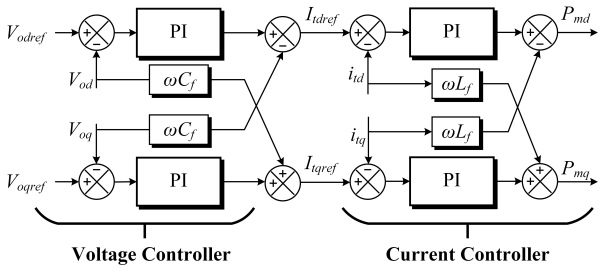


Fig. 4: Vector controller of WFVSCs.

## III. Design of Perturbation Observer-based Nonlinear Adaptive Feedback Linearization Control

In this section, the propsoed PONC will be introduced, as shown in Fig. 5. The key components of PONC are the HGOB and the FLC. The FLC is used to obtain the equivalent input-ouput model of WFVSCs and GSVSCs. Then the HGOB is designed based on the equivalent model to estimate the states and perturbations, which could be further exploited by the feedback controller to compensate the perturbations and achieve robust dynamic performance.

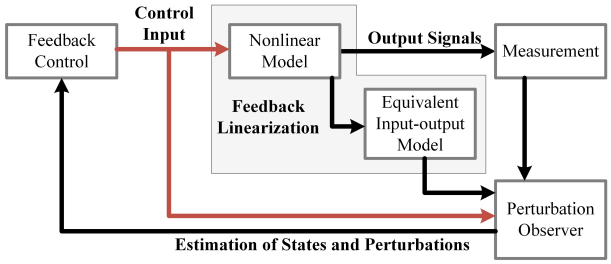


Fig. 5: The overall structure of the proposed PONC.

### A. Nonlinear Model of VSC-stations

Based on (1) and (2), the nonlinear model of a VSC-station can be described as (1−2):

$$\begin{cases} \dot{\mathbf{x}} = \mathbf{f}(\mathbf{x}) + \mathbf{k}(\mathbf{x})\mathbf{D} + \mathbf{g}(\mathbf{x})\mathbf{u} \\ \mathbf{y} = \mathbf{h}(\mathbf{x}) \end{cases} \tag{4}$$

where $\mathbf{x}$ is the state vector $\mathbf{x} = [V_{eq}, I_{in}, I_{td}, I_{tq}, V_{od}, V_{oq}, I_{od}, I_{oq}]^T$. The measured disturbance vector $\mathbf{D} = [V_{dc}, V_{gd}, V_{gq}]^T$. The control input signals are $\mathbf{u} = [P_{md}, P_{mq}]^T$, which determine the $d$- and $q$-axis components of ac-terminal voltage of VSC-stations, i.e., $V_{td}$ and $V_{tq}$.

The output signals of WFVSCs and GSVSCs can be chosen according to their specific control targets. The main objectives of WFVSCs are regulating the ac voltages of OWFs. GSVSCs can operate in two modes, i.e., dc voltage control mode and power control mode. Both of the modes rely on the regulation of $dq$-currents at PCC. Thus, the output signals of WFVSCs are the voltage errors, i.e., $\mathbf{y}^{wf} = [y_1^{wf}, y_2^{wf}]^T = [V_{od} - V_{odref}, V_{oq} - V_{oqref}]^T$ and that of GSVSCs are the current errors, i.e., $\mathbf{y}^{gs} = [y_1^{gs}, y_2^{gs}]^T = [I_{od} - I_{odref}, I_{oq} - I_{oqref}]^T$, where the superscripts '$wf$' and '$gs$' indicate the variables related to WFVSCs and GSVSCs.

### B. FLC of Wind Farm Side VSC-Stations

The basic idea of the FLC is to design a controller such that the nonlinearities of the original system can be canceled by the control input signals. Consequently, the closed-loop system is transformed into a linear one and the linear control approaches can be used to design the feedback controller. To achieve a satisfactory control performance, the relationship between the output signals $\mathbf{y}^{wf}$ and the control input signals $\mathbf{u}^{wf}$ need to be investigated firstly.

Differentiating $\mathbf{y}^{wf}$ with respect to time two times can yields the relationship between $\mathbf{y}^{wf}$ and $\mathbf{u}^{wf}$, which indicates that the relative degree of WFVSCs is $r^{wf} = 2$.

$$\ddot{\mathbf{y}}^{wf} = L_{\mathbf{f}}^2\mathbf{h}^{wf} + L_{\mathbf{g}}L_{\mathbf{f}}\mathbf{h}^{wf}\mathbf{u}^{wf} = \boldsymbol{\alpha}^{wf} + \boldsymbol{\beta}^{wf} \cdot \mathbf{u}^{wf} \tag{5}$$

where $L_{\mathbf{f}}^2\mathbf{h}^{wf}$ and $L_{\mathbf{g}}L_{\mathbf{f}}\mathbf{h}^{wf}$ are the Lie derivatives, which are given by $L_{\mathbf{f}}^2\mathbf{h}^{wf} = \boldsymbol{\alpha}^{wf} = [\alpha_d^{wf}, \alpha_q^{wf}]^T$, $L_{\mathbf{g}}L_{\mathbf{f}}\mathbf{h}^{wf} = \boldsymbol{\beta}^{wf} = [\beta_d^{wf}, 0; 0, \beta_q^{wf}]$,

$$\begin{cases} \alpha_d^{wf} = -\dfrac{R_f}{L_fC_f}I_{td} + \dfrac{2\omega}{C_f}I_{tq} - (\dfrac{L_f + L_g}{L_gL_fC_f} - \omega^2)V_{od} \\ \qquad + \dfrac{R_g}{L_gC_f}I_{od} - \dfrac{2\omega}{C_f}I_{oq} + \dfrac{2}{L_gC_f}V_{gd} - \ddot{V}_{odref} \\ \alpha_q^{wf} = -\dfrac{2\omega}{C_f}I_{td} - \dfrac{R_f}{L_fC_f}I_{tq} + -(\dfrac{L_f + L_g}{L_gL_fC_f} + \omega^2)V_{oq} \\ \qquad + \dfrac{2\omega}{C_f}I_{od} + \dfrac{R_g}{L_gC_f}I_{oq} + \dfrac{1}{L_gC_f}V_{gq} - \ddot{V}_{oqref} \\ \beta_d^{wf} = \beta_q^{wf} = \dfrac{V_{eq}}{L_fC_f} \end{cases} \tag{6}$$

To obtain the linear dynamics of the closed-loop system, the control input signals can be designed as

$$\mathbf{u}^{wf} = (\mathbf{v}^{wf} - \boldsymbol{\alpha}^{wf})/\boldsymbol{\beta}^{wf} \tag{7}$$

where $\mathbf{v}^{wf} = [v_d^{wf}, v_q^{wf}]^T$ are the auxiliary control input signals to be designed. Thus, the nonlinearities in (5) are canceled by (7) and the relationships between the output signals of WFVSCs and the auxiliary inputs are described by simple double-integrator:

$$\ddot{\mathbf{y}}^{wf} = \mathbf{v}^{wf} = [v_d^{wf}, v_q^{wf}]^T \tag{8}$$

Define new state variables $z_{d1}^{wf}=y_1^{wf}$, $z_{d2}^{wf}=\dot{y}_1^{wf}$, $z_{q1}^{wf}=y_2^{wf}$, $z_{q2}^{wf}=\dot{y}_2^{wf}$. Linear system (8) can be rewritten as

$$\begin{cases}\dot{\mathbf{z}}_d^{wf}=\mathbf{A}_d^{wf}\mathbf{z}_d^{wf}+\mathbf{B}_d^{wf}v_d^{wf}\\ \dot{\mathbf{z}}_q^{wf}=\mathbf{A}_q^{wf}\mathbf{z}_q^{wf}+\mathbf{B}_q^{wf}v_q^{wf}\end{cases}\tag{9}$$

where $\mathbf{z}_d^{wf}=[z_{d1}^{wf},z_{d2}^{wf}]$, $\mathbf{z}_q^{wf}=[z_{q1}^{wf},z_{q2}^{wf}]$; $\mathbf{A}_d^{wf}=\mathbf{A}_q^{wf}=[0,1;0,0]$, $\mathbf{B}_d^{wf}=\mathbf{B}_q^{wf}=[0,1]^T$ .

Eq. (9) indicates that the original nonlinear model of WFVSCs is transformed into the equivalent linearized system. Consequently, the linear control techniques can be employed to achieve satisfactory performance. Since the $d$- and $q$-axis subsystems in (9) are decoupled and has similar dynamics, the generalized auxiliary input signal can be derived by using the boundary tracking theory:

$$v_i^{wf}=-k_{i2}^{wf}z_{i2}^{wf}-k_{i1}^{wf}z_{i1}^{wf},i=d,q\tag{10}$$

where "$i=d,q$" indicates the variables of $d$- or $q$-axis subsystems of WFVSCs; $k_{i1}^{wf}$ and $k_{i2}^{wf}$ are the feedback control gains.

Substituting (10) into (8) yields the tracking error dynamics:

$$\ddot{z}_{i1}^{wf}+k_{i2}^{wf}\dot{z}_{i1}^{wf}+k_{i1}^{wf}z_{i1}^{wf}=0\tag{11}$$

To ensure the error dynamics (11) ares exponentially stable, $k_{i2}^{wf}$ and $k_{i1}^{wf}$ should be positive constants to place the poles of (11) at the left-hand-side of the complex plane, which can be achieved by several techniques, e.g., pole-placement method and quadratic optimal control.

Substituting (10) into (7) yields the completed nonlinear control laws of WFVSCs as follows:

$$u_i^{wf}=(-k_{i2}^{wf}z_{i2}^{wf}-k_{i1}^{wf}z_{i1}^{wf}-\alpha_i^{wf})/\beta_i^{wf}\tag{12}$$

### C. FLC of Grid Side VSC-Stations

The GSVSCs have a hierarchical control architecture, which includes a classical dc voltage droop control as the outer controller and the proposed PONC as the inner controller. The outer controller regulates dc-link voltage and power sharing between GSVSCs by generating the current reference for the inner controller. The inner controller pursues fast and robust regulation of output currents.

*1) Outer controller*

DC voltage droop control is an effective control strategy for achieving both dc voltage regulation and power allocation between GSVSCs. The classical dc voltage droop control is given as

$$P_{oref}^{gs}=P_{oref0}^{gs}+K_v^{gs}(V_{dc}^{gs}-V_{dcref}^{gs})\tag{13}$$

where the superscript '$gs$' indicates the variables related to GSVSCs; $P_{oref}^{gs}$ and $P_{oref0}^{gs}$ are the initial and final power reference of GSVSCs; $K_v^{gs}$ is the droop coefficient; $V_{dcref.i}^{gs}$ is the dc voltage reference.

Subsequently, the current reference $I_{odqref}^{gs}$ can be calculated for the inner controller. The phase-locked loop (PLL) ensures that the steady-sate voltage vector at PCC is aligned with the $d$-axis, i.e., $V_{od}^{gs}=V_o^{gs}$ and $V_{oq}^{gs}=0$. According to (3), the current reference of GSVSCs can be calculated as

$$I_{odref}^{gs}=\frac{P_{oref}^{gs}}{V_{od}^{gs}},\ I_{oqref}^{gs}=-\frac{Q_{oref}^{gs}}{V_{od}^{gs}}\tag{14}$$

*2) Inner Controller Based on FLC*

The fast current tracking is the fundamental functionality of the inner controller. To achieve the satisfactory tracking performance of $I_{odq}^{gs}$, the relationship between the output signals $I_{od}^{gs}$, $I_{oq}^{gs}$ and the control input signals $P_{md}^{gs}$, $P_{mq}^{gs}$ need to be investigated firstly, which can be obtained by differentiating $I_{od}^{gs}$, $I_{oq}^{gs}$ three times.

$$\dddot{\mathbf{y}}^{gs}=L_{\mathbf{f}}^3\mathbf{h}^{gs}+L_{\mathbf{g}}L_{\mathbf{f}}^2\mathbf{h}^{gs}\mathbf{u}^{gs}=\boldsymbol{\alpha}^{wf}+\boldsymbol{\beta}^{wf}\cdot\mathbf{u}^{wf}\tag{15}$$

where $L_{\mathbf{f}}^3\mathbf{h}^{gs}=\boldsymbol{\alpha}^{gs}=[\alpha_d^{gs},\alpha_q^{gs}]^T$, $L_{\mathbf{g}}L_{\mathbf{f}}^2\mathbf{h}^{gs}=\boldsymbol{\beta}^{gs}=[\beta_d^{gs},0;0,\beta_q^{gs}]$, which are given in (16). Eq. (15) indicates that the relative degree of GSVSCs is $r^{gs}=3$.

Similar to WFVSCs, the following control inputs can be designed to simplify the dynamics of GSVSCs:

$$\mathbf{u}^{gs}=(\mathbf{v}^{gs}-\boldsymbol{\alpha}^{gs})/\boldsymbol{\beta}^{gs}\tag{17}$$

Subsequently, the relationships between the output signals of GSVSCs and the auxiliary inputs are described by the triple-integrator:

$$\dddot{\mathbf{y}}^{gs}=\mathbf{v}^{gs}=[v_d^{gs},v_q^{gs}]^T\tag{18}$$

Define new state variables $z_{d1}^{gs}=y_1^{gs}$, $z_{d2}^{gs}=\dot{y}_1^{gs}$, $z_{d3}^{gs}=\ddot{y}_1^{gs}$, $z_{q1}^{gs}=y_2^{gs}$, $z_{q2}^{gs}=\dot{y}_2^{gs}$, $z_{q3}^{gs}=\ddot{y}_2^{gs}$. The linear system (18) can be rewritten as

$$\begin{cases}\dot{\mathbf{z}}_d^{gs}=\mathbf{A}_d^{gs}\mathbf{z}_d^{gs}+\mathbf{B}_d^{gs}v_d^{gs}\\ \dot{\mathbf{z}}_q^{gs}=\mathbf{A}_q^{gs}\mathbf{z}_q^{gs}+\mathbf{B}_q^{gs}v_q^{gs}\end{cases}\tag{19}$$

where $\mathbf{z}_d^{gs}=[z_{d1}^{gs},z_{d2}^{gs},z_{d3}^{gs}]$; $\mathbf{z}_q^{gs}=[z_{q1}^{gs},z_{q2}^{gs},z_{q3}^{gs}]$; $\mathbf{A}_d^{gs}=\mathbf{A}_q^{gs}=[0,1,0;0,0,1;0,0,0]$, $\mathbf{B}_d^{gs}=\mathbf{B}_q^{gs}=[0,0,1]^T$.

Similar to WFVSCs, Eq. (19) indicates that the original nonlinear model of GSVSCs is transformed into the equivalent linearized system. The generalized auxiliary input signal can be derived by using the boundary tracking theory:

$$v_i^{gs}=-k_{i3}^{gs}z_{i3}^{gs}-k_{i2}^{gs}z_{i2}^{gs}-k_{i1}^{gs}z_{i1}^{gs},i=d,q\tag{20}$$

where "$i=d,q$" indicates the variables of $d$- or $q$-axis subsystems of GSVSCs; $k_{i1}^{gs}-k_{i3}^{gs}$ are the feedback control gains.

Substituting (20) into (18) yields the dynamics of the tracking error:

$$\dddot{z}_{i1}^{gs}+k_{i3}^{gs}\ddot{z}_{i1}^{gs}+k_{i2}^{gs}\dot{z}_{i1}^{gs}+k_{i1}^{gs}z_{i1}^{gs}=0\tag{21}$$

$k_{i1}^{gs}-k_{i3}^{gs}$ should be positive constants such that the poles of (21) are located at the left-hand-side of the complex plane.

Substituting (20) into (17) yields the completed nonlinear control laws of GSVSCs as follows:

$$u_i^{gs}=(-k_{i3}^{gs}z_{i3}^{gs}-k_{i2}^{gs}z_{i2}^{gs}-k_{i1}^{gs}z_{i1}^{gs}-\alpha_i^{gs})/\beta_i^{gs}\tag{22}$$

### D. Perturbation Observer

The feedback control laws presented in (12) and (22) are hard to be implemented since the components $\alpha_i^{wf}$ and $\alpha_i^{gs}$

$$
\begin{cases}
\alpha_d^{gs} = -\dfrac{L_gR_f+L_fR_g}{L_g^2L_fC_f}I_{td} + \dfrac{3\omega}{L_gC_f}I_{tq} - \dfrac{3\omega R_g}{L_g^2}V_{oq} + \dfrac{2L_gR_g+3\omega^2L_g^2R_gC_f-R_g^3C_f}{L_g^3C_f}I_{od} \\
\quad + \dfrac{3\omega C_fR_g^2-3\omega L_g-\omega^3L_g^2C_f}{L_g^2C_f}I_{oq} + \dfrac{L_fC_fR_g^2-L_fL_g-L_g^2-3\omega^2L_g^2L_fC_f}{L_g^3L_fC_f}V_{od} \\
\quad - \dfrac{1}{L_g}\ddot{V}_{gd} - \dfrac{R_g+\omega L_g}{L_g^2}\dot{V}_{gd} + \dfrac{L_g+\omega^2L_g^2C_f-C_fR_g^2}{L_g^3C_f}V_{gd} + \dfrac{\omega}{L+g}\dot{V}_{gq} - \dfrac{\omega R_g}{L_g^2}V_{gq} + \dddot{V}_{odref} \\
\alpha_q^{gs} = -\dfrac{3\omega}{L_gC_f}I_{td} - \dfrac{L_gR_f+L_fR_g}{L_g^2L_fC_f}I_{tq} + \dfrac{3\omega R_g}{L_g^2}V_{od} + \dfrac{3\omega L_g+\omega^3L_g^2C_f-3\omega C_fR_g^2}{L_g^2C_f}I_{od} \\
\quad + \dfrac{2L_gR_g+3\omega^2L_g^2R_gC_f-R_g^3C_f}{L_g^3C_f}I_{oq} + \dfrac{L_fC_fR_g^2-L_fL_g-L_g^2-3\omega^2L_g^2L_fC_f}{L_g^3L_fC_f}V_{oq} \\
\quad - \dfrac{1}{L_g}\ddot{V}_{gq} - \dfrac{R_g+\omega L_g}{L_g^2}\dot{V}_{gq} + \dfrac{\omega^2L_g^2C_f-L_g-C_fR_g^2}{L_g^3C_f}V_{gq} + \dfrac{\omega}{L+g}\dot{V}_{gd} - \dfrac{\omega R_g}{L_g^2}V_{gd} + \dddot{V}_{oqref} \\
\beta_d^{gs} = \beta_q^{gs} = \dfrac{1}{L_gL_fC_f}
\end{cases} \tag{16}
$$

are complicated, as shown in (6) and (16), and is sensitive to several perturbations, such as the unmodeling dynamics, parameter uncertainties, and external disturbances. All these factors can be modeled as a lumped perturbation, which can be estimated by HGOB. The lumped perturbation $p$ can be defined as

$$p = \alpha + (\beta - \beta_0)u \tag{23}$$

where $\beta_0$ is the nominal value of $\beta$. Eqs. (5) and (15) can be rewritten as

$$
\begin{cases}
\ddot{\mathbf{y}}^{wf} = \mathbf{p}^{wf} + \boldsymbol{\beta_0}^{wf}\mathbf{u}^{wf} \\
\ddot{\mathbf{y}}^{gs} = \mathbf{p}^{gs} + \boldsymbol{\beta_0}^{gs}\mathbf{u}^{gs}
\end{cases} \tag{24}
$$

where $\mathbf{p}$ is the perturbation matrix, i.e., $\mathbf{p}^{wf} = [p_d^{wf}, 0; 0, p_q^{wf}]$ and $\mathbf{p}^{gs} = [p_d^{gs}, 0; 0, p_q^{gs}]$; $\boldsymbol{\beta_0}$ is the nominal input matrix, i.e., $\boldsymbol{\beta_0}^{wf} = [\beta_{d0}^{wf}, 0; 0, \beta_{q0}^{wf}]$ and $\boldsymbol{\beta_0}^{gs} = [\beta_{d0}^{gs}, 0; 0, \beta_{q0}^{gs}]$.

A new state $z_{n+1} = p$ is augmented to represent the lumped perturbations. Subsequently, Eqs. (9) and (19) can be rewritten by generalized form:

$$
\begin{cases}
\dot{\mathbf{z}}_i^{wf} = \mathbf{A}_i^{wf}\mathbf{z}_i^{wf} + \mathbf{B}_i^{wf}(z_{i3}^{wf} + \beta_{i0}^{wf}u_i^{wf}) \\
\dot{z}_{i3}^{wf} = \dot{p}_i^{wf}
\end{cases}, i = d, q \tag{25}
$$

$$
\begin{cases}
\dot{\mathbf{z}}_i^{gs} = \mathbf{A}_i^{gs}\mathbf{z}_i^{gs} + \mathbf{B}_i^{gs}(z_{i4}^{wf} + \beta_{i0}^{gs}u_i^{gs}) \\
\dot{z}_{i4}^{gs} = \dot{p}_i^{gs}
\end{cases}, i = d, q \tag{26}
$$

where "$i = d, q$" indicates the $d$- or $q$-axis subsystems of WFVSCs and GSVSCs.

Assume that the measurements of $V_{od}, V_{oq}$ of WFVSCs and $I_{od}, I_{oq}$ of GSVSCs are available. The HGOBs of WFVSCs and GSVSCs are designed as

$$
\begin{cases}
\dot{\hat{\mathbf{z}}}_i^{wf} = \mathbf{A}_i^{wf}\hat{\mathbf{z}}_i^{wf} + \mathbf{B}_i^{wf}\hat{v}_i^{wf} + \mathbf{H}_i^{wf}(z_{i1}^{wf} - \hat{z}_{i1}^{wf}) \\
\dot{\hat{z}}_{i3}^{wf} = \dfrac{h_{i3}^{wf}}{\varepsilon^3}(z_{i1}^{wf} - \hat{z}_{i1}^{wf})
\end{cases} \tag{27}
$$

$$
\begin{cases}
\dot{\hat{\mathbf{z}}}_i^{gs} = \mathbf{A}_i^{gs}\hat{\mathbf{z}}_i^{gs} + \mathbf{B}_i^{gs}\hat{v}_i^{gs} + \mathbf{H}_i^{gs}(z_{i1}^{gs} - \hat{z}_{i1}^{gs}) \\
\dot{\hat{z}}_{i4}^{gs} = \dfrac{h_{i4}^{gs}}{\varepsilon^4}(z_{i1}^{gs} - \hat{z}_{i1}^{gs})
\end{cases} \tag{28}
$$

where the embellishment '$\hat{}$' indicates the estimated value; $\varepsilon$ is a small constant, which meets $0 < \varepsilon \ll 1$; $\mathbf{H}_i^{wf} = [\frac{h_{i1}^{wf}}{\varepsilon}, \frac{h_{i2}^{wf}}{\varepsilon^2}]^T$ and $\mathbf{H}_i^{gs} = [\frac{h_{i1}^{gs}}{\varepsilon}, \frac{h_{i2}^{gs}}{\varepsilon^2}, \frac{h_{i3}^{gs}}{\varepsilon^3}]^T$; $h_{i1}^{gs} - h_{i4}^{gs}$ and $h_{i1}^{wf} - h_{i3}^{wf}$ are observer gain constants, which should be chosen such that the polynomials $s^3 + h_{i1}^{wf}s^2 + h_{i2}^{wf}s + h_{i3}^{wf} = 0$ and $s^4 + h_{i1}^{gs}s^3 + h_{i2}^{gs}s^2 + h_{i3}^{gs}s + h_{i4}^{gs} = 0$ should be Hurwitz.

With the estimated perturbations $\hat{z}_{i3}^{wf}$, $\hat{z}_{i4}^{gs}$, the control input (12) and (22) can be modified as

$$
\begin{cases}
u_i^{wf} = (-k_{i2}^{wf}\hat{z}_{i2}^{wf} - k_{i1}^{wf}\hat{z}_{i1}^{wf} - \hat{z}_{i3}^{wf})/\beta_{i0}^{wf} \\
u_i^{gs} = (-k_{i3}^{gs}\hat{z}_{i3}^{gs} - k_{i2}^{gs}\hat{z}_{i2}^{gs} - k_{i1}^{gs}\hat{z}_{i1}^{gs} - \hat{z}_{i4}^{gs})/\beta_{i0}^{gs}
\end{cases} \tag{29}
$$

The block diagram of the proposed controller is shown in Figs. 6. Note that only the $d$-axis controllers are given because $q$-axis controllers have the similar structure. The measurements required by the proposed controllers of WFVSCs and GSVSCs are only the $V_{od}, V_{oq}$ and $V_{dc}^{gs}, I_{od}, I_{oq}$. Compared with the traditional FLC and VC strategies, much fewer measurements are required by the proposed controller, and the system uncertainties and disturbances can be compensated by the HGOB. Owing to the inherent limits of converters, the current references $I_{odref}^{gs}$ and $I_{oqref}^{gs}$ obtained from the outer controllers and the control inputs $u_d^{wf}, u_q^{wf}, u_d^{gs}$ and $u_q^{gs}$ must be bounded. The setting of the bound values will be introduced in Section V.

## IV. Stability Analysis

The stability of the proposed PONC is investigated in this section. The closed-loop systems and the dynamics of the observer errors should be modeled first [33].

The estimation error of HGOBs of WFVSCs and GSVSCs can be defined as $\tilde{z}_{ij}^k = z_{ij}^k - \hat{z}_{ij}^k$, and their scaled estimation

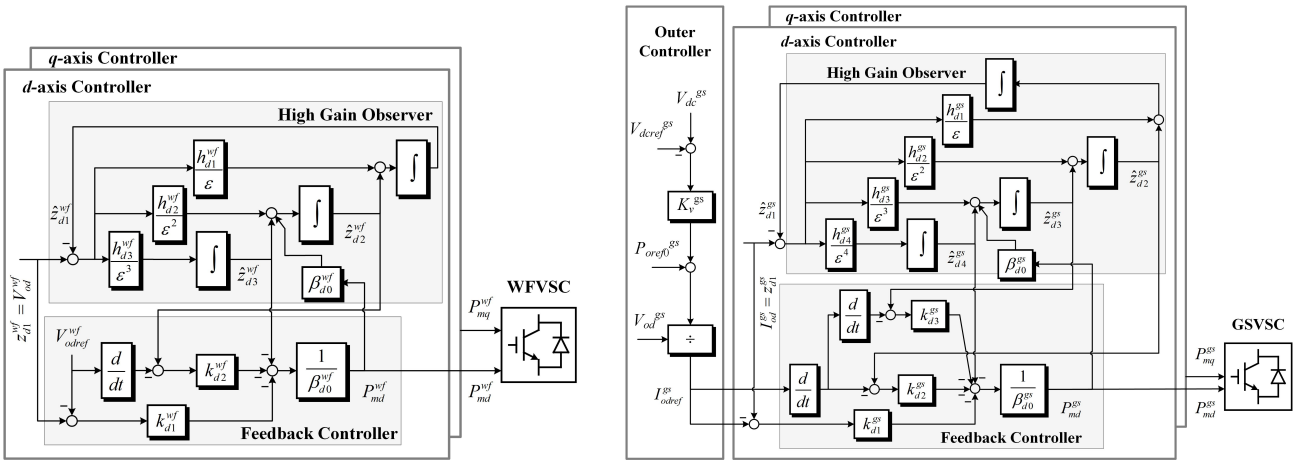


(a) The controller of WFVSCs.

(b) The controller of GSVSCs.

Fig. 6: The block diagram of the proposed controllers.

error are defined as

$$\begin{cases} \eta_{i1}^{wf} = \dfrac{\tilde{z}_{i1}^{wf}}{\varepsilon^2}, \eta_{i2}^{wf} = \dfrac{\tilde{z}_{i2}^{wf}}{\varepsilon}, \eta_{i3}^{wf} = \tilde{z}_{i3}^{wf} \\ \eta_{i1}^{gs} = \dfrac{\tilde{z}_{i1}^{gs}}{\varepsilon^3}, \eta_{i2}^{gs} = \dfrac{\tilde{z}_{i2}^{gs}}{\varepsilon^2}, \eta_{i3}^{gs} = \dfrac{\tilde{z}_{i3}^{gs}}{\varepsilon}, \eta_{i4}^{gs} = \tilde{z}_{i1}^{gs} \end{cases} \tag{30}$$

Hence, we have $[\hat{\mathbf{z}}_i^{wf}; \hat{z}_{i3}^{wf}] = [\mathbf{z}_i^{wf}; z_{i3}^{wf}] - \mathbf{D}_i^{wf}(\varepsilon)\boldsymbol{\eta}_i^{wf}$ and $[\hat{\mathbf{z}}_i^{gs}; \hat{z}_{i4}^{gs}] = [\mathbf{z}_i^{gs}; z_{i4}^{gs}] - \mathbf{D}_i^{gs}(\varepsilon)\boldsymbol{\eta}_i^{gs}$, where $\boldsymbol{\eta}_i^{wf} = [\eta_{i1}^{wf}, \eta_{i2}^{wf}, \eta_{i3}^{wf}]^T$, $\boldsymbol{\eta}_i^{gs} = [\eta_{i1}^{gs}, \eta_{i2}^{gs}, \eta_{i3}^{gs}, \eta_{i4}^{gs}]^T$, $\mathbf{D}_i^{wf}(\varepsilon) = \text{block diag}[\varepsilon^2, \varepsilon, 1]$, $\mathbf{D}_i^{gs}(\varepsilon) = \text{block diag}[\varepsilon^3, \varepsilon^2, \varepsilon, 1]$. Then the control inputs (29) can be rewritten as

$$\begin{cases} u_i^{wf} = \dfrac{1}{\beta_{i0}^{wf}}(-k_{i2}^{wf} z_{i2}^{wf} - k_{i1}^{wf} z_{i1}^{wf} - z_{i3}^{wf} \\ \qquad + \mathbf{K}_i^{wf}\mathbf{D}_i^{wf}(\varepsilon)\boldsymbol{\eta}_i^{wf}) \\ u_i^{gs} = \dfrac{1}{\beta_{i0}^{gs}}(-k_{i3}^{gs} z_{i3}^{gs} - k_{i2}^{gs} z_{i2}^{gs} - k_{i1}^{gs} z_{i1}^{gs} - z_{i4}^{gs} \\ \qquad + \mathbf{K}_i^{gs}\mathbf{D}_i^{gs}(\varepsilon)\boldsymbol{\eta}_i^{gs}) \end{cases} \tag{31}$$

where $\mathbf{K}_i^{wf} = [k_{i2}^{wf}, k_{i1}^{wf}, 1]$, $\mathbf{K}_i^{gs} = [k_{i3}^{gs}, k_{i2}^{gs}, k_{i1}^{gs}, 1]$.

Substituting (31) into (25) and (26) yields the closed-loop dynamics of the equivalent linear systems with HGOBs

$$\begin{cases} \dot{\mathbf{z}}_i^{wf} = \mathbf{A}_{iz}^{wf}\mathbf{z}_i^{wf} + \mathbf{B}_i^{wf}\mathbf{K}_i^{wf}\mathbf{D}_i^{wf}(\varepsilon)\boldsymbol{\eta}_i^{wf} \\ \dot{\mathbf{z}}_i^{gs} = \mathbf{A}_{iz}^{gs}\mathbf{z}_i^{gs} + \mathbf{B}_i^{gs}\mathbf{K}_i^{gs}\mathbf{D}_i^{gs}(\varepsilon)\boldsymbol{\eta}_i^{gs} \end{cases} \tag{32}$$

where $\mathbf{A}_{iz}^{wf} = \mathbf{A}_i^{wf} - \mathbf{B}_i^{wf} \cdot [k_{i1}^{wf}, k_{i2}^{wf}]$, $\mathbf{A}_{iz}^{gs} = \mathbf{A}_i^{gs} - \mathbf{B}_i^{gs}[k_{i1}^{gs}, k_{i2}^{gs}, k_{i3}^{gs}]$.

The dynamics of the observer errors can be derived by (30), (25) $-$(28):

$$\begin{cases} \varepsilon\dot{\boldsymbol{\eta}}_i^{wf} = \mathbf{A}_{i\eta}^{wf} + \varepsilon\mathbf{B}_{i\eta}^{wf}\dot{p}_i^{wf} \\ \varepsilon\dot{\boldsymbol{\eta}}_i^{gs} = \mathbf{A}_{i\eta}^{gs} + \varepsilon\mathbf{B}_{i\eta}^{gs}\dot{p}_i^{gs} \end{cases} \tag{33}$$

where $\mathbf{A}_{i\eta}^{wf} = [-h_{i1}^{wf}, 1, 0; -h_{i2}^{wf}, 0, 1; -h_{i3}^{wf}, 0, 0]$, $\mathbf{A}_{i\eta}^{gs} = [-h_{i1}^{gs}, 1, 0, 0; -h_{i2}^{gs}, 0, 1, 0; -h_{i3}^{gs}, 0, 0, 1; -h_{i4}^{gs}, 0, 0, 0]$, $\mathbf{B}_{i\eta}^{wf} = [0, 0, 1]^T$, $\mathbf{B}_{i\eta}^{gs} = [0, 0, 0, 1]^T$.

One can observe from (32) and (33) that the closed-loop systems and the observer errors of WFVSCs and GSVSCs have the similar formats, which can be represented by

$$\begin{cases} \dot{\mathbf{z}}_i^j = \mathbf{A}_{iz}^j\mathbf{z}_i^j + \mathbf{B}_i^j\mathbf{K}_i^j\mathbf{D}_i^j(\varepsilon)\boldsymbol{\eta}_i^j \\ \varepsilon\dot{\boldsymbol{\eta}}_i^j = \mathbf{A}_{i\eta}^j + \varepsilon\mathbf{B}_{i\eta}^j\dot{p}_i^j \end{cases}, j = wf, gs \tag{34}$$

where "$j = wf, gs$" indicates the models of WFVSCs or GSVSCs. In the following analysis, (34) will be employed.

Assumption 1: The lumped perturbation $p_i^j$ and its derivatives $\dot{p}_i^j$ in (34) are Lipschitz in their arguments and bounded over the domain of interest.

Assumption 2: The zero dynamics of WFVSCs and GSVSCs are exponentially stable and the original operating point is a stable equilibrium point.

A Lyapunov function candidate can be defined for the generalized system (34) as

$$V_i^j(z, \eta) = W_{iz}^j + W_{i\eta}^j \tag{35}$$

where $W_{iz}^j = \boldsymbol{z}_i^{jT}\mathbf{P}_{iz}^j\boldsymbol{z}_i^j$ over a ball $B(0, o_i^j) \subset R^3$, for some $o_i^j > 0$, and $W_{i\eta}^j = \boldsymbol{\eta}_i^{jT}\mathbf{P}_{i\eta}^j\boldsymbol{\eta}_i^j$; $\mathbf{P}_{iz}$ and $\mathbf{P}_{i\eta}$ are the positive definite matrices, which can be calculated by $\mathbf{P}_{iz}^j\mathbf{A}_{iz}^j + \mathbf{A}_{iz}^{jT}\mathbf{P}_{iz}^j = -\mathbf{I}_{iz}^j$ and $\mathbf{P}_{i\eta}^j\mathbf{A}_{i\eta}^j + \mathbf{A}_{i\eta}^{jT}\mathbf{P}_{i\eta}^j = -\mathbf{I}_{i\eta}^j$.

Choose $\xi_i^j < o_i^j$; then, given Assumption 2, we have, $\forall(\mathbf{z}_i^j, \eta_i^j) \in B(0, \xi_i^j) \times (\|\eta_i^j \le \xi_i^j\|) = \Lambda_i^j, |\dot{p}_i^j| \le d_i^j$, where $d_i^j$ is the upper bound of $\dot{p}_i^j$. It can be shown that $\forall(\mathbf{z}_i^j, \eta_i^j) \in \Lambda_i^j$, than, we have

$$\begin{aligned} \dot{V}_i^j(z, \eta) &= \frac{\partial W_{iz}^j}{\partial \mathbf{z}_i^j}\dot{\mathbf{z}}_i^j + \frac{\partial W_{i\eta}^j}{\partial \mathbf{z}_i^j}\dot{\boldsymbol{\eta}}_i^j \\ &\le -\|\mathbf{z}_i^j\|^2 - \frac{1}{\varepsilon}\|\boldsymbol{\eta}_i^j\|^2 + 2\|\mathbf{z}_i^j\|\|\mathbf{P}_{iz}^j\mathbf{K}_i^j\|\|\boldsymbol{\eta}_i^j\| \\ &\quad + 2\|\boldsymbol{\eta}_i^j\|\|\mathbf{P}_{i\eta}^j\|d_i^j \\ &\le -\|\mathbf{z}_i^j\|(\|\mathbf{z}_i^j\| - 2\|\mathbf{P}_{iz}^j\mathbf{K}_i^j\|\|\boldsymbol{\eta}_i^j\|) \\ &\quad - \|\boldsymbol{\eta}_i^j\|(\frac{1}{\varepsilon}\|\boldsymbol{\eta}_i^j\| - 2\|\mathbf{P}_{i\eta}^j\|d_i^j) \end{aligned} \tag{36}$$

Defining $\xi_{i\eta}^j = 2\varepsilon\|\mathbf{P}_{i\eta}^j\|d_i^j$ and $\xi_{iz}^j = 2\|\mathbf{P}_{iz}^j\mathbf{K}_i^j\|\xi_{i\eta}^j = 4d_i^j\varepsilon\|\mathbf{P}_{i\eta}^j\|\|\mathbf{P}_{iz}^j\|$; Then, for any given $\xi_i^j < o_i^j$, we can choose $\varepsilon^* = \min\{\frac{\xi_i^j}{8d_i^j\|\mathbf{P}_{i\eta}^j\|\|\mathbf{P}_{iz}^j\|}, \frac{\xi_i^j}{4d_i^j\|\mathbf{P}_{i\eta}^j\|}\}$. Then $\forall\varepsilon$, $0 < \varepsilon < \varepsilon^*$, $\|\mathbf{z}_i^j\| \le \xi_i^j/2$, $\|\boldsymbol{\eta}_i^j\| \le \xi_i^j/2$, $\|\mathbf{z}_i^j\| \ge \xi_{iz}^j$, and $\|\boldsymbol{\eta}_i^j\| \ge \xi_{i\eta}^j$, such

that

$$\begin{aligned}\dot{V}_i^j(z,\eta) &\le -\|\mathbf{z}_i^j\|(\|\mathbf{z}_i^j\| - 2\|\mathbf{P}_{iz}^j\|\|\mathbf{K}_i^j\|\|\boldsymbol{\eta}_i^j\|) \\ &\quad - \|\boldsymbol{\eta}_i^j\|(\frac{1}{\varepsilon}\|\boldsymbol{\eta}_i^j\| - 2\|\mathbf{P}_{i\eta}^j\|d_i^j) \\ &\le -\|\mathbf{z}_i^j\|(\|\mathbf{z}_i^j\| - \xi_{iz}^j) - \|\boldsymbol{\eta}_i^j\|(\|\boldsymbol{\eta}_i^j\| - \xi_{i\eta}^j) \le 0\end{aligned} \tag{37}$$

Hence, there is $T_1(\xi_i^j)$ and $T_1 > 0$, it can be shown that

$$\|\mathbf{z}_i^j\| + \|\boldsymbol{\eta}_i^j\| \le \xi_i^j, \forall t > T_1 \tag{38}$$

Thus, the above analysis indicates that the closed-loop systems and estimation error (34) are bounded under the proposed PONC (27) − (29).

## V. Case Study I

A 5-terminal VSC-MTDC system shown in Fig. 7 is used to validate the effectiveness of the proposed PONC controller in DIgSILENT/PowerFactory 15.20. WFVSC1 and WFVSC2 connect with two offshore wind farms, and GSVSC1−3 connect with three equivalent onshore ac grids. The capacities of WFVSCs and GSVSCs are 500MVA and 300MVA, respectively. The nominal ac- and dc-terminal voltages are 110kV and 500kV. Each OWF consists of with 60 Doubly fed Induction Generator (DFIG) based wind turbines and the total wind power is 300MW. Both the WFVSCs and GSVSCs adopt the proposed controllers. The equivalent $\pi$ model is used for modeling the dc cables. All the parameters of the test system including the PONCs, WFVSCs, GSVSCs, and dc cables are given in Table I. The voltage and current references shown in Fig.6 are bounded as $0.95 \le |V_{odref}^{gs}| \le 1.05, |V_{oqref}^{gs}| = 0$, $|I_{odref}^{gs}| \le 1.2$ and $|I_{oqref}^{gs}| \le 1.2$. The control inputs are bounded as $|u_d^{wf}| \le 1, |u_q^{wf}| \le 1, |u_d^{gs}| \le 1$ and $|u_q^{gs}| \le 1$. EMT simulation kernel and 'A-stable' numerical integration algorithm of PowerFactory are utilized to solve electromagnetic transient simulations [43]. The simulation time step and sampling step are 0.001s. To test the damping performance of the proposed PONC, multiple events are considered:

a) The step changes of the voltage reference of WFVSC1 and the current reference of GSVSC2 are applied at $t = 0.1$s, respectively.
b) A three-phase short-circuit fault near the ac terminal of GSVSC2 occurs at $t = 0.1$s and is cleared at $t = 0.2$s.
c) The power outputs of OWFs fluctuate continuously.

Event a) is used to test the tracking performance of PONC. Event b) tests the dynamic performance of PONC under the continuous change of system operating points, and event c) is used to test the dynamic performance of PONC under complex operating scenarios. Note that all the uncertainties of the system parameters are considered in these test events. A quantitative index $S_x$ is defined to explicitly evaluate the performance of the proposed controller.

$$S_x = \int_{t_1}^{t_2} |f(\tau) - f_{ref}(\tau)| d\tau \tag{39}$$

where $x$ is the variable of interest; $f$ and $f_{ref}$ represent the value and the reference of $x$; $t_1$ and $t_2$ are the beginning time and the end time of the simulation. A large $S_x$ signifies a weak reference tracking performance and high sensitivity to perturbations when a specific controller is employed.

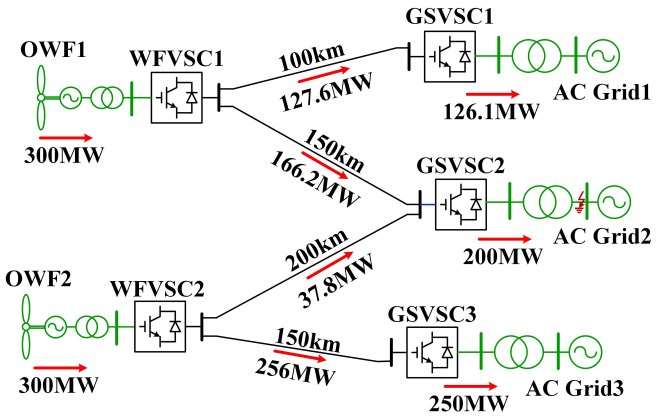


Fig. 7: The single diagram of the test system.

TABLE I: Parameters of the Test System

| WFVSCs | GSVSCs |
|---|---|
| **VSC-stations** | |
| $R_{arm}^{wf}$ = 1.5Ω, $L_{arm}^{wf}$ = 60mH<br>$C_{eq}^{wf}$ = 100μF, $R_f^{wf}$ = 0.7Ω<br>$L_f^{wf}$ = 11.9mH, $C_f^{wf}$ = 20μF<br>$R_g^{wf}$ = 0.1Ω, $L_g^{wf}$ = 15.92mH | $R_{arm}^{gs}$ = 0.9Ω, $L_{arm}^{gs}$ = 45mH<br>$C_{eq}^{gs}$ = 100μF, $R_f^{gs}$ = 1Ω<br>$L_f^{gs}$ = 19.8mH, $C_f^{gs}$ = 10μF<br>$R_g^{gs}$ = 0.2Ω, $L_g^{gs}$ = 23.87mH |
| **PONC** | |
| $k_{d1,i}^{wf} = k_{q1,i}^{wf} = 1 \times 10^6$<br>$k_{d2,i}^{wf} = k_{q2,i}^{wf} = 2 \times 10^2$<br>$h_{1,i}^{wf} = 1 \times 10^3$, $h_{2,i}^{wf} = 3 \times 10^5$<br>$h_{3,i}^{wf} = 1 \times 10^7$, $\varepsilon_i^{wf} = 0.01$ | $k_{d1,i}^{gs} = k_{q1,i}^{gs} = 1 \times 10^9$<br>$k_{d2,i}^{gs} = k_{q2,i}^{gs} = 3 \times 10^6$<br>$k_{d3,i}^{gs} = k_{q3,i}^{gs} = 3 \times 10^3$<br>$h_{1,i}^{gs} = 3 \times 10^2$, $h_{2,i}^{gs} = 1.5 \times 10^6$<br>$h_{3,i}^{gs} = 5 \times 10^8$, $h_{4,i}^{gs} = 6.25 \times 10^{10}$<br>$\varepsilon_i^{gs} = 0.01$, $K_{v,1}^{gs}$ = 20p.u.<br>$K_{v,2}^{gs}$ = 20p.u., $K_{v,2}^{gs}$ = 20p.u. |
| **DC transmission line** | |
| Resistance: 0.0113Ω/km, Inductance: 0.45mH/km, Capacitance: 0.28μF/km | |

### A. Step Change of AC-Terminal Voltage of WFVSC1

The $d$-axis voltage reference of WFVSC1, i.e., $V_{odref,1}^{wf}$, is decreased from 1.018p.u. to 0.95p.u at $t = 0.1$s. To test the performance of PONC with system uncertainties, the value of $L_f$ used in PONC of WFVSC1 is 10mH larger than the real LCL-filter, i.e., $\Delta L_f = 10$mH. The system responses are shown in Figs. 8 and 9. $V_{od}^{wf}$ and $V_{oq}^{wf}$ of WFVSC1 are utilized to calculate the quantitative indices $S_{vod1}$ and $S_{voq1}$, respectively, as shown in Table II.

TABLE II: Quantitative Indices of Case a

| | $S_{vod}$ | $S_{voq}$ |
|---|---|---|
| PONC | 2.2 | 0.16 |
| VC | 14.68 | 26.26 |

It can be observed from Fig. 8 that the $V_{od,1}^{wf}$ has a satisfactory dynamic response with the control of PONC. The $V_{od,1}^{wf}$ decreases to its reference within 15ms. The $V_{oq,1}^{wf}$ is

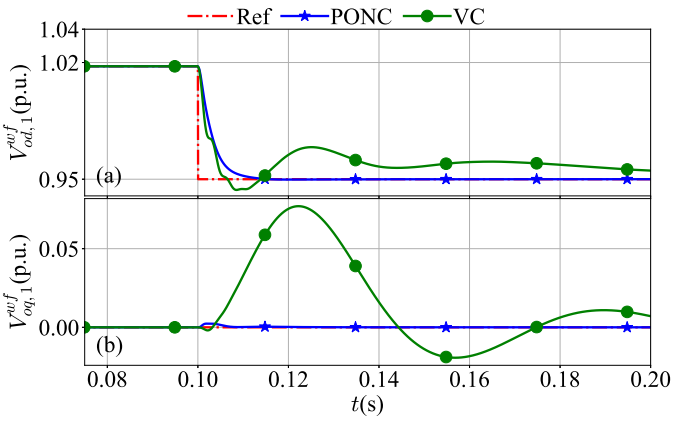


Fig. 8: Responses of (a) $V_{od,1}^{wf}$ and (b) $V_{oq,1}^{wf}$.

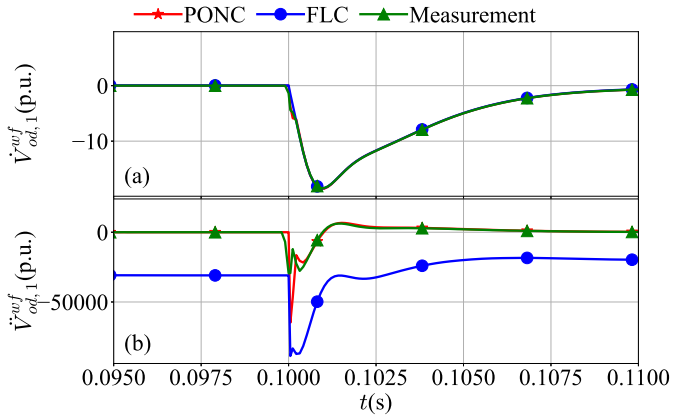


Fig. 9: Responses of (a) $\dot{V}_{od,1}^{wf}$ and (b) $\ddot{V}_{od,1}^{wf}$.

slightly influenced since the cross-coupling of $dq$-components is well compensated by PONC. Whilst $V_{od,1}^{wf}$ spend more time to decrease to the reference and the dynamics of $V_{oq,1}^{wf}$ is more oscillatory when PI controller is used. Fig. 9 shows that the estimation of $\dot{V}_{od,1}^{wf}$ is close to the first-order derivative of the measurements by either PONC or FLC. Large estimation error of $\ddot{V}_{od,1}^{wf}$ is introduced by $\Delta L_f$ when FLC is used. Whilst the PONC has a better performance because the impact of $\Delta L_f$ on $\ddot{V}_{od,1}^{wf}$ can be well-compensated by PONC.

Table II shows that $S_{vod1}$ and $S_{voq1}$ with PONC are much lower than that with VC controller, which means that the proposed PONC has better voltage tracking performance and the $dq$-axis voltage decoupling performance.

### *B. Step Change of the Output Current of GSVSC2*

The $d$-axis current reference of GSVSC2, i.e., $I_{odref,2}^{gs}$, is decreased from 1.02p.u. to 0.95p.u at $t = 0.1$s. To test the performance of PONC with system uncertainties, the value of $C_f$ used in PONC of GSVSC2 is 5$\mu$F larger than the real LCL-filter, i.e., $\Delta C_f = 5\mu$H. The system responses are shown in Figs. 10 and 11. $I_{od}^{gs}$ and $I_{oq}^{gs}$ of GSVSC2 are utilized to calculate the quantitative indices $S_{iod2}$ and $S_{ioq2}$ , respectively, as shown in Table III.

Fig. 10 indicates that the $I_{od,2}^{gs}$ rises to the new reference rapidly without overshoot when PONC is adopted. The $I_{oq,2}^{gs}$

TABLE III: Quantitative Indices of Case b

| | $S_{iod2}$ | $S_{ioq2}$ |
|---|---|---|
| PONC | 2.55 | 0.52 |
| VC | 3.94 | 2.7 |

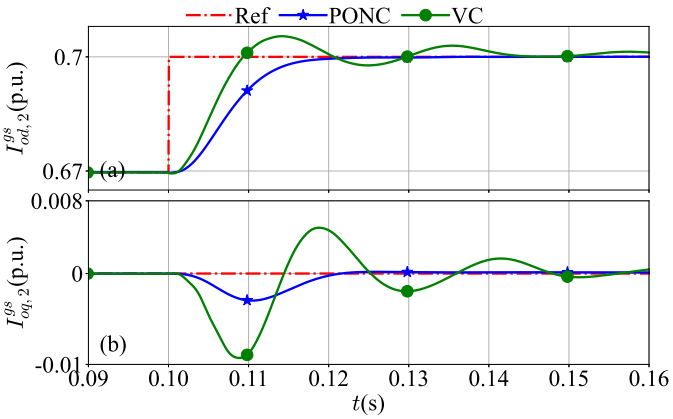


Fig. 10: Responses of (a) $I_{od,2}^{gs}$ and (b) $I_{oq,2}^{gs}$.

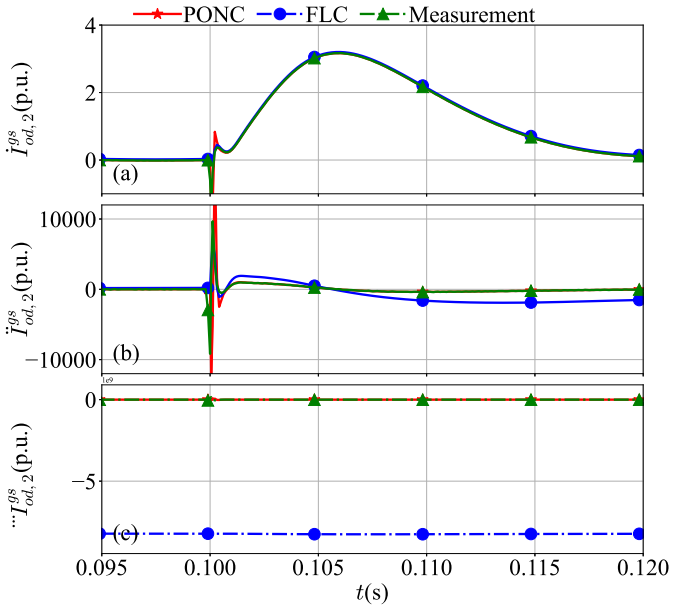


Fig. 11: Responses of (a) $\dot{I}_{od,2}^{gs}$ and (b) $\ddot{I}_{od,2}^{gs}$.

is slightly influenced because of the decoupling of the $dq$-components. Whilst the step responses of $I_{od,2}^{gs}$ with PI controller is more oscillatory and $I_{oq,1}^{wf}$ is affected significantly due to the cross-coupling effect. As observed in Fig. 11, $\Delta C_f$ has little influence on the estimation of $\dot{I}_{od,2}^{gs}$ when either PONC or FLC is adopted. The estimation error of $\ddot{I}_{od,2}^{gs}$ by FLC is little large than that by PONC. This error is further augmented by the FLC in the estimation of $\dddot{I}_{od,2}^{gs}$ and is far larger than the measurements. Hence, PONC has a better estimation performance with parameter uncertainties.

Table III shows that $S_{iod2}$ and $S_{ioq2}$ with PONC are much lower than that with VC controller, which means that the proposed PONC has better current tracking performance and

the $dq$-axis current decoupling performance.

### C. Fault Ride Though Capability

To test the fault ride through capability of the proposed PONC, a three-phase fault is applied on the transmission line between GSVSC2 and ac grid 2 at $t = 0.1$s and is cleared at $t = 0.2$s. The parameter uncertainties are $\Delta C_{f,i}^{gs} = 5\mu$H, $\Delta L_{f,i}^{gs} = 10$mH. The system responses are shown in Figs. 12 $-$ 15. Since the dc voltage deviations between GSVSCs are generally small, only the dc voltage of GSVSC2 is shown in 13. The magnitudes of ac voltage, dc voltage, active power output and the reactive power output of GSVSC2 are utilized to calculate the quantitative indices $S_{vo2}$, $S_{vdc2}$, $S_{po2}$ and $S_{qo2}$, respectively, as shown in Table IV.

TABLE IV: Quantitative Indices of Case c

| | $S_{vo2}$ | $S_{vdc2}$ | $S_{po2}$ | $S_{qo2}$ |
|---|---|---|---|---|
| PONC | 976.88 | 25.3 | 729.26 | 194.26 |
| VC | 1081.55 | 103.9 | 1646.51 | 744.78 |

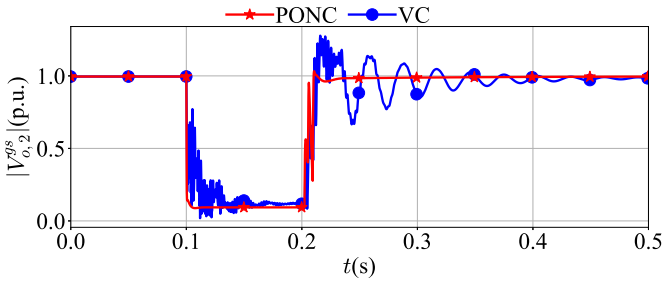


Fig. 12: Magnitudes of ac voltages at PCC of GSVSC2.

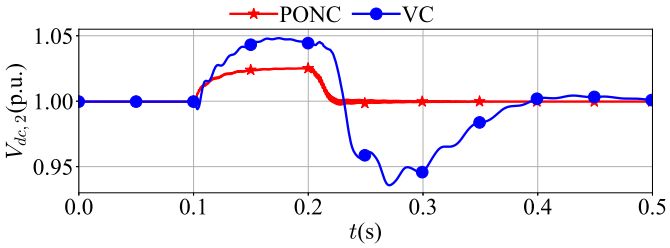


Fig. 13: DC voltage of GSVSC2.

The ac-side fault has serious impacts on both the ac and dc voltage. During the fault period, the voltage magnitude $|V_{o,2}^{gs}|$ drops to zero, and the power output of GSVSC2 is blocked [see Fig. 12 and Fig. 14(b)]. Hence, the dc voltage soars because of the imbalance between the power input of WFVSCs and the power output of GSVSCs, as shown in Fig. 13. PONC has a such stable power regulation ability that the power output of GSVSC2 is reallocated to GSVSC1 and GSVSC3 quickly with the help of dc voltage droop control [see the red curves in Fig. 14]. Hence the dc voltage deviation is limited by PONC. Although the dc voltage droop control is also embedded in VC controller, its power regulation ability is slightly weaker than PONC so that the power imbalance in the dc grid leads

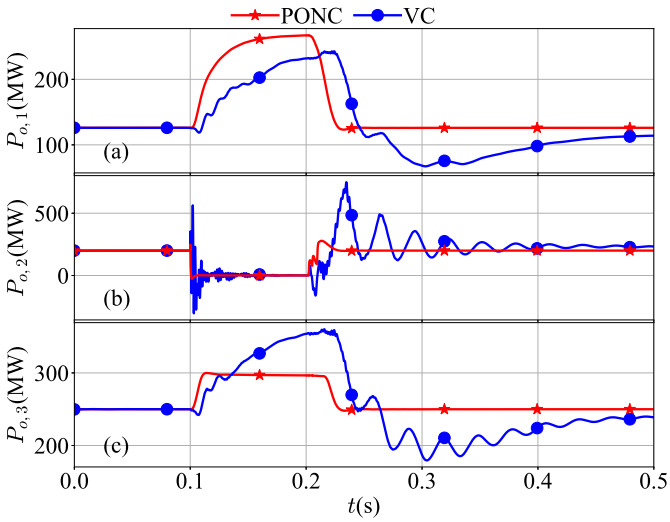


Fig. 14: The active power outputs of GSVSCs (a) GSVSC1; (b) GSVSC2; (c) GSVSC3.

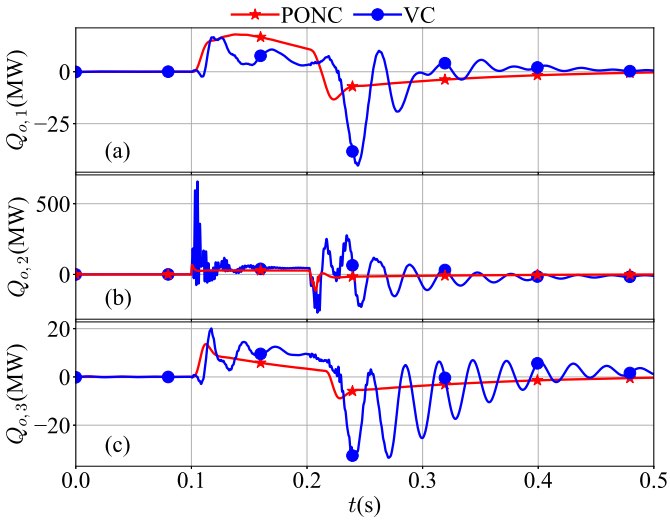


Fig. 15: The reactive power outputs of GSVSCs (a) GSVSC1; (b) GSVSC2; (c) GSVSC3.

to more severe dc voltage deviation, which has reached to the upper and lower limits, i.e., $\pm 0.05p.u.$ [see the blue curve in Fig. 13].

After the fault is cleared, the ac and dc votlage can restore to the pre-fault value due to the fast and stable regulation of power output of GSVSCs by PONC [see the red curves in Figs. 12 and 13]. Whilst the severe power oscillations of VC controller, which have exceed the rated capacity of GSVSCs, result in the long-term recovery of ac and dc voltage [see the blue curves in Figs. 14 and 15].

Table IV shows that the quantitative indices with PONC are much lower than that with VC controller, which means that the transient period is shorter and the oscillations decay quicker when the proposed PONC is employed. Hence PONC has better fault ride though capability when ac faults occur.

### D. Wind Power Fluctuation

To test the performance of PONC under continuous-varying conditions, the power outputs of OWFs are considered to be time-chaning, which are given in Fig. 16. The system responses are shown in Figs. 17- 19. The $V_{od}^{wf}$, $V_{oq}^{wf}$ of WFVSC1 and $V_{dc}$ of GSVSC1 are used to calculate the quantitative indices $S_{vod1}$, $S_{voq1}$ and $S_{vdc1}$, respectively, as shown in Table V.

TABLE V: Quantitative Indices of Case d

| | $S_{vod1}$ | $S_{voq1}$ | $S_{vdc1}$ |
|---|---|---|---|
| PONC | 1.30 | 7.64 | 42.59 |
| VC | 528.60 | 260.27 | 135.87 |

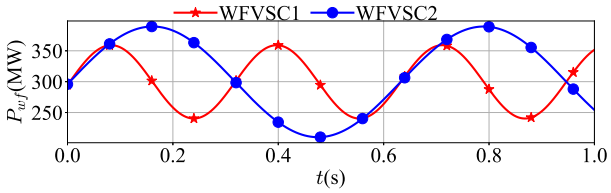


Fig. 16: The power outputs of OWFs.

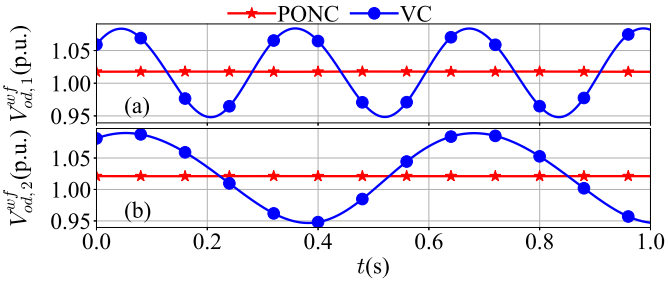


Fig. 17: The $d$-axis voltages of WFVSCs: (a) WFVSC1; (b) WFVSC2.

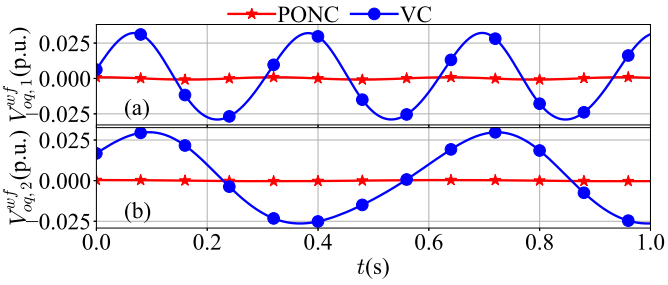


Fig. 18: The $q$-axis voltages of WFVSCs: (a) WFVSC1; (b) WFVSC2.

It can be observed from Figs. 17 and 18 that the random wind power injection slightly influence the ac voltages of WFVSCs when PONC is employed. $V_{od}^{wf}$ and $V_{oq}^{wf}$ are stabilized at the 1p.u. and 0p.u., respectively. However, the voltage regulation ability of VC controller is much weaker under the stochastic conditions. Significant fluctuations of $V_{od}^{wf}$ and $V_{oq}^{wf}$ can be observed [see the blue lines in Figs. 17 and 18].

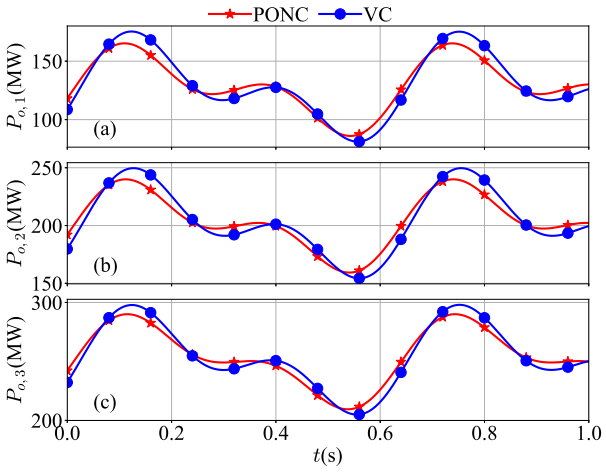


Fig. 19: The power outputs of GSVSCs.

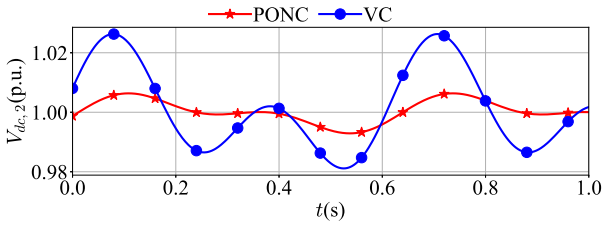


Fig. 20: DC voltage of GSVSC2.

Since dc voltages is sensitive to the power balance in dc grid, the power outputs of GSVSCs should change with the power injections of WFVSCs in time to stabilize the dc voltage. As shown in Fig. 19, the PONC could regulate the power outputs of GSVSCs more rapidly than VC controller. Hence, one can observed from Fig. 20 that the dc voltage variation is limited in a narrow range by PONC. Whilst the VC controller could lead to severe dc voltage fluctuation.

Table V shows that the quantitative indices with PONC are much lower than that with PI controller, which means that the system with PONC is more stable when the wind power is fluctuating.

## VI. Case Study II

Based on the VSC-MTDC model in Section V, a 7-terminal VSC-MTDC system shown in Fig. 21 is developed to test the performance of the proposed PONC control in large systems. OWF3, WFVSC3 and GSVSC4 are integrated into the VSC-MTDC system, and the topology of the dc grid becomes more complex. The total wind power of OWF3 is 400MW. The parameters of WFVSC3, GSVSC4 and the dc cables are the same with I. To test the fault-ride through performance of the proposed PONC, three-phase short-circuit faults which occur near the ac terminal of GSVSC2 and GSVSC3 at $t = 0.1$s and are cleared at $t = 0.2$s.

The magnitudes of ac voltage, dc voltage, active power output and the reactive power output of GSVSCs are utilized to calculate the quantitative indices $S_{vo2}$, $S_{vdc2}$, $S_{vo4}$ and $S_{vdc4}$, respectively, as shown in Table VI.

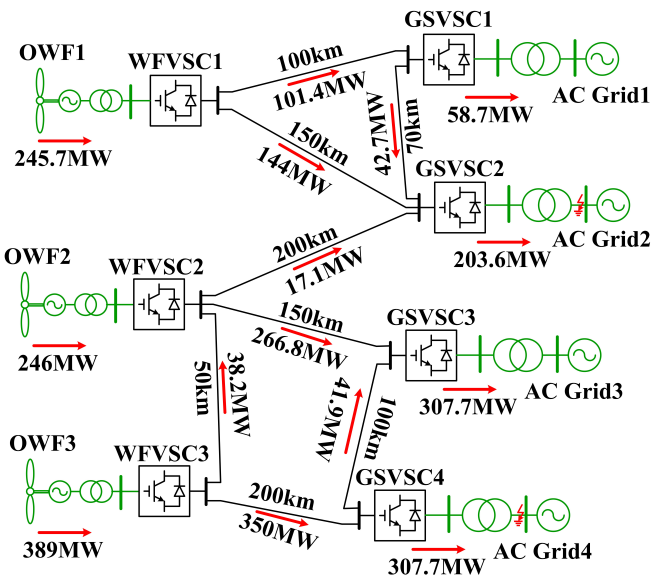


Fig. 21: The single diagram of the large system.

TABLE VI: Quantitative Indices of Case Study II

| | $S_{vo2}$ | $S_{vdc2}$ | $S_{vo4}$ | $S_{vdc4}$ |
|---|---|---|---|---|
| PONC | 550.9 | 58.6 | 539.6 | 62.1 |
| PI | 684.3 | 162.5 | 667.3 | 166 |

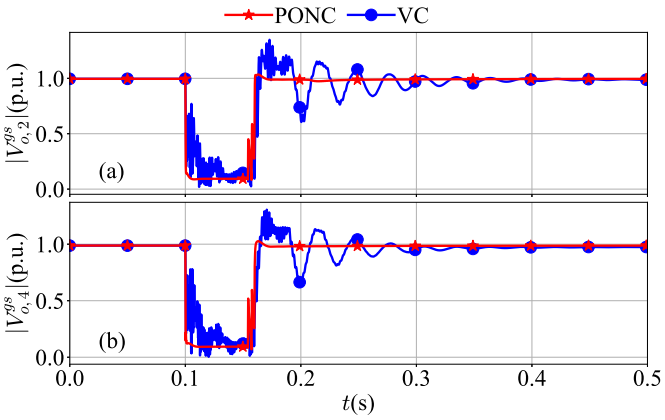


Fig. 22: Magnitudes of ac voltages at PCC of GSVSCs (a) GSVSC2; (b) GSVSC4.

The short-circuit faults of GSVSC2 and GSVSC4 lead to large voltage deviation in both the ac- and dc-side, as shown in Figs. 22 and 23. The voltage magnitudes of GSVSC2 and GSVSC4 drop to zero, and the dc voltages $|V^{gs}_{dc,2}|$ and $|V^{gs}_{dc,4}|$ have large excursions during the fault period. When PONC is employed, the dc voltage deviations are effectively limited due to its rapid power regulation. Whilst the dc voltage deviation is more severe when VC is used [see the blue curves in Fig. 23], which has exceeded the upper and lower limits, i.e., $\pm 0.05 p.u.$. After the fault is cleared, the ac and dc voltage can rapidly restore to the pre-fault value without oscillations when PONC is adopted [see the red curves in Figs. 22 and 23].

Table VI shows that the quantitative indices with PONC

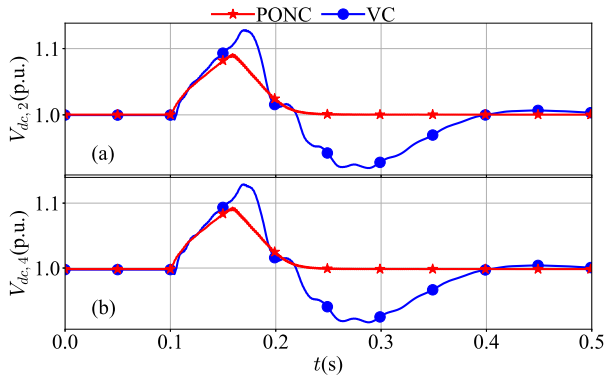


Fig. 23: DC voltages of GSVSCs (a) GSVSC2; (b) GSVSC4.

are much lower than that with PI controller, which means that the transient period is shorter and the oscillations decay quicker when the proposed PONC is employed. Hence PONC has better fault ride though capability when ac faults occur in large hybrid ac/dc power systems.

## VII. Discussion

The complex configuration and stochastic operating condition pose multiple challenges on the stability and security of VSC-MTDC systems: 1) The stochastic wind power leads to the time-varying operating points of VSC-MTDC systems, which means that the controllers should have rapid tracking performance, including current, voltage and power tracking. 2) The inherent nonlinearity introduced by the complex configuration of VSC-MDTC systems make it hard to obtain accurate system model. The parameter uncertainty and unknown dynamics are inevitable. 3) The disturbances can occur in different parts of VSC-MTDC systems, including the fluctuation of wind power, short-circuit faults in ac grids.

The conventional vector controllers use the PI compensator as the core component to regulate the voltage, current and power of converters. The parameters of VC can be tuned by bode plot, nyquist technique, root locus. However, these methods often linearize the system model at an equilibrium point, and achieve the controller parameters, which may be not applicable for all the other operating points, especially in VSC-MTDC systems with the integration of large scale wind farms.

Considering all these challenges, this paper uses the perturbation observer and feedback linearization techniques to construct the PONC for VSC-MTDC systems. A lumped perturbation term $p$ is defined in 23 to represent the comprehensive effect of unknown dynamics, parameter uncertainty, and external disturbance on system outputs. With the help of feedback linearization technique, the linear input-output relationship of converters, i.e., 5 and 15, can be derived. Based on the high gain observer, the lumped perturbation term is estimated, and its effects on the system dynamics are further compensated from the control input, i.e., 29. According to the simulations, it was illustrated that the proposed PONC can effectively improve the dynamics of VSC-MTDC systems compared with the conventional VC.

## VIII. Conclusion

This paper has investigated the design of the perturbation observer-based nonlinear adaptive feedback linearization control to improve the dynamic performance of VSC-MTDC systems against multiple uncertainties, including modeling uncertainties and external disturbances. The effectiveness of the proposed PONC was validated by nonlinear simulations. The main conclusions are summarized as follows:

a) The voltage/current tracking performance of VSC-MTDC system are improved by the proposed PONC, which could estimate and compensate the system uncertainties and unknown nonlinearities. Hence the accurate model and parameters are not required. Moreover, the $d$- and $q$-axis dynamics is decoupled by PONC, which helps to achieve better independent control of the active and reactive power.
b) The tuning of the porposed PONC is much easier than the conventional VC. Owing to the transformation of closed-loop dynamics to linear ones by PONC, there are only several parameters to be tuned, i.e., the feedback and observer gain constants, which are mainly determined by the expected control performance and are irrelevant to the system model.
c) The system dynamic performance under external disturbances are improved by the proposed PONC. The voltage fluctuation of OWFs caused by the stochastic wind energy are effectively restrained by WFVSCs, and the dc voltage deviation and the power oscillations during the short circuit faults are dampened by GSVSCs.

In our future work, we will investigate the design of secondary distributed control strategy of VSC-MTDC systems to coordinate multiple converters and to provide ancillary support to the connected ac grids for improving the overall stability of the hybrid ac/dc power systems.

## References


[1] D. Van Hertem, O. Gomis-Bellmunt, and J. Liang, *HVDC Technology and Technology for Offshore Grids*. IEEE, 2016. [Online]. Available: https://ieeexplore.ieee.org/document/7435071

[2] T. M. Haileselassie and K. Uhlen, "Power system security in a meshed north sea HVDC grid," *Proceedings of the IEEE*, vol. 101, no. 4, pp. 978–990, 2013.

[3] S. Huang, Q. Wu, Y. Guo, X. Chen, B. Zhou, and C. Li, "Distributed voltage control based on ADMM for large-scale wind farm cluster connected to VSC-HVDC," *IEEE Transactions on Sustainable Energy*, vol. 11, no. 2, pp. 584–594, 2020.

[4] W. H. Chen, J. Yang, L. Guo, and S. Li, "Disturbance-Observer-Based Control and Related Methods - An Overview," *IEEE Transactions on Industrial Electronics*, vol. 63, no. 2, pp. 1083–1095, 2016.

[5] C. Li, P. Zhan, J. Wen, M. Yao, N. Li, and W. J. Lee, "Offshore wind farm integration and frequency support control utilizing hybrid multiterminal HVDC transmission," *IEEE Transactions on Industry Applications*, vol. 50, no. 4, pp. 2788–2797, 2014.

[6] S. Sanchez, A. Garces, G. Bergna-Diaz, and E. Tedeschi, "Dynamics and stability of meshed multiterminal hvdc networks," *IEEE Transactions on Power Systems*, vol. 34, no. 3, pp. 1824–1833, 2019.

[7] J. Liang, T. Jing, O. Gomis-bellmunt, J. Ekanayake, and N. Jenkins, "Operation and Control of Multiterminal HVDC Transmission for OffshoreWind Farms," *IEEE Transactions on Power Delivery*, vol. 26, no. 4, pp. 2596–2604, 2011.

[8] K. Rouzbehi, A. Miranian, J. I. Candela, A. Luna, and P. Rodriguez, "A generalized voltage droop strategy for control of multiterminal DC grids," *IEEE Transactions on Industry Applications*, vol. 51, no. 1, pp. 607–618, 2015.

[9] M. Davari and Y. A. R. I. Mohamed, "Robust droop and DC-bus voltage control for effective stabilization and power sharing in VSC multiterminal DC grids," *IEEE Transactions on Power Electronics*, vol. 33, no. 5, pp. 4373–4395, 2018.

[10] A. Yazdani and R. Iravani, *Voltage-sourced converters in power systems*. Wiley Online Library, 2010, vol. 34.

[11] W. Wang, Y. Li, Y. Cao, U. Häger, and C. Rehtanz, "Adaptive droop control of vsc-mtdc system for frequency support and power sharing," *IEEE Transactions on Power Systems*, vol. 33, no. 2, pp. 1264–1274, 2018.

[12] S. G. Vennelaganti and N. R. Chaudhuri, "Selective power routing in mtdc grids for inertial and primary frequency support," *IEEE Trans. Power Syst.*, vol. 33, no. 6, pp. 7020–7030, 2018.

[13] ——, "Ratio-based selective inertial and primary frequency support through MTDC grids with offshore wind farms," *IEEE Transactions on Power Systems*, vol. 33, no. 6, pp. 7277–7287, 2018.

[14] M. A. Elizondo, R. Fan, H. Kirkham, M. Ghosal, F. Wilches-Bernal, D. Schoenwald, and J. Lian, "Interarea oscillation damping control using high-voltage dc transmission: A survey," *IEEE Transactions on Power Systems*, vol. 33, no. 6, pp. 6515–6923, 2018.

[15] G. Wu, Z. Du, C. Li, and G. Li, "VSC-MTDC operation adjustments for damping inter-area oscillations," *IEEE Transactions on Power Systems*, vol. 34, no. 2, pp. 1373–1382, 2019.

[16] B. Silva, C. L. Moreira, H. Leite, and J. A. Pecas Lopes, "Control strategies for AC fault ride through in multiterminal HVDC grids," *IEEE Transactions on Power Delivery*, vol. 29, no. 1, pp. 395–405, 2014.

[17] W. Sanusi, M. Al Hosani, and M. S. El Moursi, "A Novel DC Fault Ride-Through Scheme for MTDC Networks Connecting Large-Scale Wind Parks," *IEEE Transactions on Sustainable Energy*, 2017.

[18] R. Eriksson, "On the centralized nonlinear control of HVDC systems using Lyapunov theory," *IEEE Transactions on Power Delivery*, 2013.

[19] ——, "Coordinated control of multiterminal DC grid power injections for improved rotor-angle stability based on Lyapunov theory," *IEEE Transactions on Power Delivery*, 2014.

[20] J. Renedo, A. Garcia-Cerrada, A. Garcia-Cerrada, and L. Rouco, "Active power control strategies for transient stability enhancement of AC/DC grids with VSC-HVDC multi-terminal systems," *IEEE Transactions on Power Systems*, vol. 31, no. 6, pp. 1–10, 2016.

[21] J. Renedo, A. Garcia-Cerrada, and L. Rouco, "Reactive-Power Coordination in VSC-HVDC Multi-Terminal Systems for Transient Stability Improvement," *IEEE Transactions on Power Systems*, vol. 32, no. 5, pp. 3758–3767, 2017.

[22] G. Tang, Z. Xu, H. Dong, and Q. Xu, "Sliding Mode Robust Control Based Active-Power Modulation of Multi-Terminal HVDC Transmissions," *IEEE Transactions on Power Systems*, 2016.

[23] M. Benadja, M. Rezkallah, S. Benhalima, A. Hamadi, and A. Chandra, "Hardware Testing of Sliding Mode Controller for Improved Performance of VSC-HVDC Based Offshore Wind Farm under DC Fault," *IEEE Transactions on Industry Applications*, vol. 55, no. 2, pp. 2053–2063, 2019.

[24] L. Papangelis, M. Debry, P. Panciatici, and T. Van Cutsem, "Coordinated supervisory control of multi-terminal hvdc grids: A model predictive control approach," *IEEE Transactions on Power Systems*, vol. 32, no. 6, pp. 4673–4683, 2017.

[25] A. Musa, L. R. Sabug, and A. Monti, "Robust Predictive Sliding Mode Control for Multiterminal HVDC Grids," *IEEE Transactions on Power Delivery*, vol. 33, no. 4, pp. 1545–1555, 2018.

[26] Y. Guo, H. Gao, Q. Wu, H. Zhao, J. Østergaard, and M. Shahidehpour, "Enhanced voltage control of VSC-HVDC-connected offshore wind farms based on model predictive control," *IEEE Transactions on Sustainable Energy*, vol. 9, no. 1, pp. 474–487, 2018.

[27] R. Fan, R. Huang, and L. Sun, "Nonlinear model predictive control of hvdc for inter-area oscillation damping," *Electric Power Systems Research*, vol. 165, pp. 27–34, 2018.

[28] Z. Li, Q. Hao, F. Gao, L. Wu, and M. Guan, "Nonlinear decoupling control of two-terminal mmc-hvdc based on feedback linearization," *IEEE Transactions on Power Delivery*, vol. 34, no. 1, pp. 376–386, 2019.

[29] B. Yang, T. Yu, H. Shu, J. Dong, and L. Jiang, "Robust sliding-mode control of wind energy conversion systems for optimal power extraction via nonlinear perturbation observers," *Applied Energy*, vol. 210, pp. 711–723, 2018.

[30] B. Yang, T. Yu, H. Shu, D. Zhu, N. An, Y. Sang, and L. Jiang, "Perturbation observer based fractional-order sliding-mode controller for mppt of grid-connected pv inverters: Design and real-time implementation," *Control Engineering Practice*, vol. 79, pp. 105–125, 2018.

[31] B. Yang, T. Yu, X. Zhang, H. Li, H. Shu, Y. Sang, and L. Jiang, "Dynamic leader based collective intelligence for maximum power point tracking of pv systems affected by partial shading condition," *Energy Conversion and Management*, vol. 179, pp. 286–303, 2019.

[32] J. Lai, X. Yin, L. Jiang, X. Yin, Z. Wang, and Z. Ullah, "Disturbance-observer-based pbc for static synchronous compensator under system disturbances," *IEEE Transactions on Power Electronics*, vol. 34, no. 11, pp. 11 467–11 481, 2019.

[33] K. Shi, X. Yin, L. Jiang, Y. Liu, Y. Hu, and H. Wen, "Perturbation estimation based nonlinear adaptive power decoupling control for dfig wind turbine," *IEEE Transactions on Power Electronics*, vol. 35, no. 1, pp. 319–333, 2020.

[34] B. Yang, Y. Y. Sang, K. Shi, Y. Wei, L. Jiang, and T. Yu, "Design and real-time implementation of perturbation observer based sliding-mode control for vsc-hvdc systems," *Control Engineering Practice*, vol. 56, no. nov., pp. 13–26, 2016.

[35] B. Yang, L. Jiang, W. Yao, and Q. Wu, "Perturbation observer based adaptive passive control for damping improvement of multi-terminal voltage source converter-based high voltage direct current systems," *Transactions of the Institute of Measurement and Control*, vol. 39, no. 9, pp. 1409–1420, 2017.

[36] B. Yang, L. Jiang, T. Yu, H. C. Shu, C. K. Zhang, W. Yao, and Q. H. Wu, "Passive control design for multi-terminal vsc-hvdc systems via energy shaping," *International Journal of Electrical Power & Energy Systems*, vol. 98, no. JUN., pp. 496–508, 2018.

[37] K. S. Xiahou, Y. Liu, L. L. Zhang, M. S. Li, and Q. H. Wu, "Robust current sensorless control of vsc-based mtdc transmissions for integrating wind farms," *IEEE Journal of Emerging and Selected Topics in Power Electronics*, pp. 1–1, 2020.

[38] M. Darabian, A. Jalilvand, A. Ashouri, and A. Bagheri, "Stability improvement of large-scale power systems in the presence of wind farms by employing hvdc and statcom based on a non-linear controller," *International Journal of Electrical Power & Energy Systems*, vol. 120, p. 106021, 2020.

[39] L. Jiang, Q. H. Wu, and J. Y. Wen, "Decentralized nonlinear adaptive control for multimachine power systems via high-gain perturbation observer," *IEEE Transactions on Circuits and Systems I: Regular Papers*, vol. 51, no. 10, pp. 2052–2059, 2004.

[40] Y. Li, G. Tang, J. Ge, Z. He, H. Pang, J. Yang, and Y. Wu, "Modeling and Damping Control of Modular Multilevel Converter Based DC Grid," *IEEE Transactions on Power Systems*, vol. 33, no. 1, pp. 723–735, 2017.

[41] W. Wang, M. Barnes, O. Marjanovic, and O. Cwikowski, "Impact of DC breaker systems on multiterminal VSC-HVDC stability," *IEEE Transactions on Power Delivery*, vol. 31, no. 2, pp. 769–779, 2016.

[42] S. Saeid, H. Yazdi, K. Rouzbehi, J. I. Candela, J. Milimonfared, P. Rodriguez, S. S. H. Yazdi, K. Rouzbehi, J. Ignacio Candela, J. Milimonfared, and P. Rodriguez, "Flexible HVDC Transmission Systems Small Signal Modelling : A case study on CIGRE Test MT-HVDC Grid," *Proceedings IECON 2017 - 43rd Annual Conference of the IEEE Industrial Electronics Society*, pp. 256–262, 2017.

[43] D. GmbH, "Manuals DigSilent PowerFactory," 15.2 edition, 2015.